Available online at www.sciencedirect.com
SCIENCE DIRECT
International Journal of Heat and Mass Transfer 49 (2006) 1885–1895
International Journal of HEAT and MASS TRANSFER
www.elsevier.com/locate/ijhmt

Enhanced boiling heat transfer simulation from structured surfaces: Semi-analytical model

S. Murthy [a], Y. Joshi [b,*], S. Gurrum [b], W. Nakayama [c]

[a] John Welch Technology Center, GE Research, Bangalore 560 066, India
[b] G.W. Woodruff School of Mechanical Engineering, Georgia Institute of Technology, Atlanta, GA 30332, USA
[c] ThermTech International, Kanagawa 255-0004, Japan

Received 14 October 2004; received in revised form 28 October 2005
Available online 19 January 2006

Abstract

A semi-analytical model of the bubble dynamics is proposed based on the experimental results reported in the literature on boiling from porous enhanced surfaces. The model considers the 'flooded mode' regime of enhancement boiling and is validated for data covering a range of tunnel and pore dimensions. The dynamic model accounts for the temporal evaporation rate variation inside tunnels to arrive at the latent heat flux due to internal evaporation and frequency of bubble formation. The population density is predicted using an empirical formulation, and in turn used to estimate the total heat flux from the porous enhanced surface. The model predicts the heat flux for pool boiling from structured surfaces within ±30% of the experimental data. The model is subsequently used in the prediction of the thermal performance of a novel two-phase heat spreader that employs porous structured surfaces for enhancing boiling heat transfer.

1. Introduction

Nucleate boiling from porous structured surfaces results in high heat transfer rates with very small rise in the surface temperature. This knowledge has been used extensively [1] to improve the performance of heat exchangers and process equipment, through the use of enhanced tubes for promoting boiling/condensation heat transfer process. Despite the vast body of research on boiling from such enhanced surfaces [2], the fundamental physical mechanisms involved are far from being well understood. Visualization studies have been carried out in the past to ascertain nucleate boiling mechanism from structured surfaces [3–7].

Nakayama et al. [8] proposed three possible modes of boiling from structured surfaces, namely the 'flooded' mode, the 'suction–evaporation mode' and the 'dried-up mode' (Fig. 1). Based on the above observations of boiling modes, Webb and Haider [9], Chien and Webb [10] and Ramaswamy et al. [11], have proposed mechanistically based models to predict boiling performance of structured surfaces. Webb's model is based on the 'flooded' mode regime and assumes alternate zones of liquid and vapor slugs in the sub-surface tunnels. Though the model developed was independent of empirical constants, its application was limited to structures with a continuous slot at the top of the sub-surface tunnels.

Chien and Webb [10] and Ramaswamy et al. [11] focus on the 'suction–evaporation' mode of boiling from enhanced surfaces. Their models require the specification of the Hamaker constant for calculating the liquid saturation temperature. Chien's model assumes the Hamaker constant value for R-113 to be 2.0×10^{-12} J, while Ramaswamy's model uses a value of 1×10^{-13} J for FC-72. Ramaswamy et al. [11] note that their model is highly sensitive to the value of the Hamaker constant used, thereby requiring its accurate evaluation. Dasgupta et al. [12] carried out experiments to determine the equilibrium disjoining pressure from thin evaporating menisci and found that the Hamaker constant is a function of the liquid surface combination and the wall superheat value. For an octane/silicon system, the Hamaker constant was measured

* Corresponding author. Tel.: +1 40 4 385 2810; fax: +1 40 4 894 8496.
E-mail address: yogendra.joshi@me.gatech.edu (Y. Joshi).

0017-9310/$ - see front matter © 2005 Elsevier Ltd. All rights reserved.
doi:10.1016/j.ijheatmasstransfer.2005.10.035

Nomenclature

C_{tg}	empirical constant for growth rate
C_h	Hamaker constant (J)
c_p	specific heat of liquid (J/kg-K)
D	diameter (m)
F	force (N)
f	frequency (Hz)
h_{fg}	latent heat of vaporization (J/kg)
k	thermal conductivity (W/m-K)
L	length of thin-film region
Q''	heat flux (W/m^2)
m	mass (kg)
n_s	nucleation site density (m^{-2})
Pr	Prandtl number
p	pressure (Pa)
R	instantaneous bubble radius
r_t	tunnel radius
T_w	wall temperature (°C)
T_{sat}	saturation temperature (°C)
t	time (s)
ΔT_{sup}	wall superheat
V	volume (m^3)
u	velocity (m/s)
v	velocity (m/s)
x_m	mean length of liquid slug (m)

Greek symbols

σ	surface tension (N/m)
θ	contact angle (degrees)
ρ	density
δ	film thickness (μm)
δ_0	initial film thickness (μm)

Subscripts

B	buoyancy
b	bubble
bi	bubble inertia
ex	external
f	film
L	lift
l	liquid
m	menisci
max	maximum
min	minimum
mom	momentum
ne	non-evaporating
p	pore
sat	saturation
t	tunnel
ug	unsteady growth
v	vapor

to be in the range $3.0–0.69 \times 10^{-21}$ J for wall superheats in the range 0.000045–0.002 °C. More generally, the Hamaker constant for two macroscopic phases interacting across a medium can be derived using the Lifshitz theory of van der Waals forces [13]. The above theory, when used in calculating the Hamaker constant for CCl_4/copper system, results in a value of 1.18×10^{-19} J. Substituting a value of 10^{-19} J for the Hamaker constant in [10,11] results in very large discrepancies between the predicted results and the experimental data available in the literature for boiling from enhanced surfaces. Moreover, both [10,11] are based on thin-film evaporation across the meniscii along the corners of the enhancement feature and fail to account for observed boiling enhancement from circular sub-surface tunnels where no such meniscii exist.

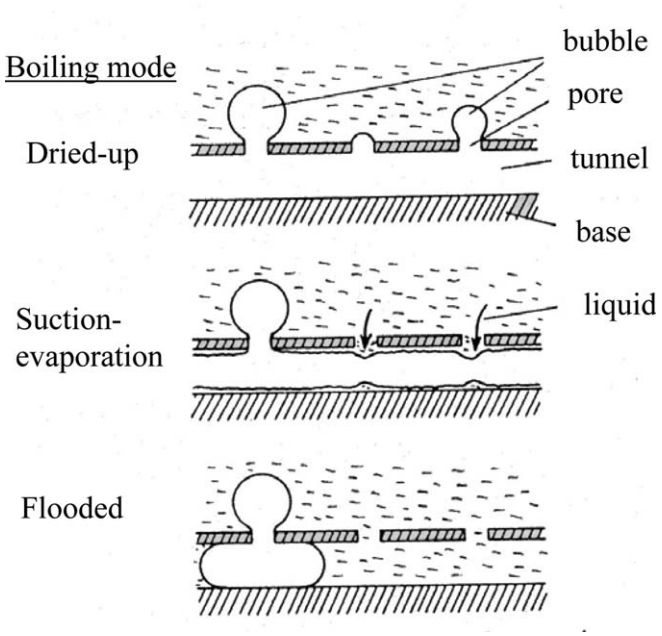

Fig. 1. Possible modes of boiling (Nakayama et al. [8]).

Visualization experiments performed by Nakayama et al. [4] and Arshad and Thome [5] show the existence of an advancing liquid–vapor interface in the re-entrant cavities of the enhancement structure. More recently, Ghiu et al. [14] carried out visualization studies on transparent enhancement structures similar to those used by Nakayama et al. [4]. Their experiments confirmed the presence of alternating liquid–vapor slug regions in the sub-surface tunnels of the enhancement structure.

The current study presents a unified model for the bubble dynamics from porous structures and compares the predic-

tions with experimental results reported in the literature. Boiling from enhanced surfaces is quantified by predicting the bubble departure diameter, bubble frequency, nucleation site density and dissipated heat flux. Modeling of these parameters is outlined in Section 2. Section 3 compares the model predictions with experimental results reported in the literature and the conclusions are presented in Section 4.

2. Semi-analytical model

The semi-analytical model developed captures the boiling of highly wetting liquids from structured surfaces with sub-surface tunnels having circular cross section. The model can be used for predicting the performance of tunnels with other cross sections by representing these with circular tunnels of same wetted perimeter. The model assumes the existence of a spherical bubble inside the sub-surface tunnel at the start of a bubble departure cycle (Fig. 2a). Evaporation at the liquid–vapor interface across the two menisci, and the intermediate thin liquid film cause the vapor plug to expand within the tunnel (Fig. 2b). The vapor expansion occurs in the tunnel until the pressure force is greater than the surface tension force on the pore ($4\sigma/d_p$) (Fig. 2c). At this point, bubble growth occurs outside the tunnel (Fig. 2d), until the detaching forces overcome the forces that keep the bubble attached to the enhanced surface.

The departure diameter is obtained based on a balance of the static and dynamic forces acting on a bubble. Bubble frequency is defined as the inverse of the total time for one bubble cycle and is calculated based on the time taken for a bubble to reach its departure diameter. The heat dissipated through evaporation inside the tunnels (Q''_t) is combined with the enhanced convection on external surfaces (Q''_{ex}) for arriving at the total heat flux. The nucleation site density (n_s) or the total number of bubbles formed per unit area is required for computing the total heat flux and is obtained through an empirical correlation.

2.1. Modeling bubble departure diameter

Most existing models for bubble departure from structured surfaces consider only the static forces acting during bubble growth. Nakayama et al. [15] developed an empirical correlation for bubble departure through the balance of buoyancy and surface tension forces. Webb and Haider [9] replaced the empirical constant in Nakayama's model by introducing the contact angle θ in the formulation. More recently, Ramaswamy et al. [11] accounted for the effect of dynamic forces in their bubble departure model.

The mechanism of bubble growth for structured surfaces involves evaporation of the liquid menisci inside the sub-surface tunnels of the enhancement structure. The present model for bubble departure assumes the departing bubbles to be spherical in shape and attached to the surface pore during the bubble growth. The departure diameter is predicted by including the effect of the static and dynamic forces acting on the bubble. The buoyancy force and the lift flux force tend to pull the bubble off the pore, while the growth force, the surface tension force and the bubble inertia force keep it attached. The bubble departure diameter is obtained by solving the force balance equation

$$F_{ug} + F_{st} + F_{bi} = F_B + F_L \tag{1}$$

The expressions used for the forces in the force balance study are identical to those derived in Ramaswamy et al. [11].

2.2. Modeling tunnel heat transfer

The tunnel heat flux during one bubble cycle of frequency f is calculated based on the liquid evaporation from the thin film (Q''_f) and the two menisci at each end of a vapor plug (Q''_m) in the tunnel. Evaporation from the thin film occurs until the non-evaporating film thickness is reached wherein the inter-molecular forces between the solid tunnel wall and the liquid in the thin film creates an energy barrier that hinders further evaporation. The non-evaporating thickness is calculated by [10]

$$\delta_{ne} = \left(\frac{C_h T_{sat}}{\rho_l h_{fg} \Delta T_{sup}}\right)^{1/3} \tag{2}$$

where the Hamaker constant C_h accounts for the disjoining pressure. Since all the heat transferred to the vapor zone is

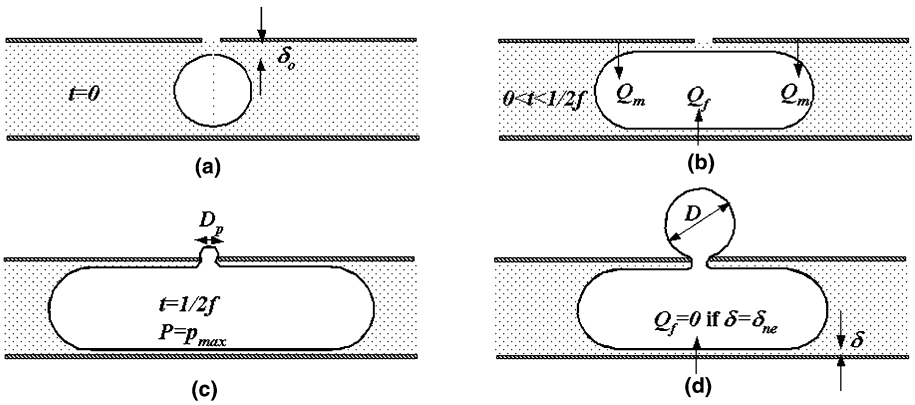

Fig. 2. Envisioned bubble formation and departure in the 'flooded' mode regime.

latent, the tunnel heat flux (Q''_t) equals the latent heat of the vapor contained in a bubble and is given by

$$Q''_t = \int_0^{1/f} (2Q''_m + Q''_f)\,dt = \frac{\pi}{6}\rho_v h_{fg} D_b^3 \tag{3}$$

2.3. Modeling bubble frequency

The bubble frequency f is obtained by solving Eq. (3) through modeling of thin film (Q''_f) and meniscus (Q''_m) heat transfer rates. Q''_m is obtained through calculation of the radial heat conduction and is given by (Fig. 3)

$$\begin{aligned} Q''_m &= 2\pi k_l (T_w - T_{sat}) \int_0^{r_t-\delta} \frac{dx}{\ln\left(\frac{r_t}{\sqrt{(r_t-\delta)^2 - x^2}}\right)} \\ &= 2\pi k_l (T_w - T_{sat})(r_t - \delta) \int_0^1 \frac{d\xi}{\ln\left(\frac{r_t}{(r_t-\delta)\sqrt{1-\xi^2}}\right)} \\ &\quad \left(\text{where } \xi = \frac{x}{(r_t-\delta)}\right) \\ &= 4\pi r_t k_l (T_w - T_{sat}) \sqrt{\frac{r_t}{2\delta}} \tan^{-1}\left(\sqrt{\frac{r_t}{2\delta}}\right) \quad (\text{for } \delta \ll r_t) \end{aligned} \tag{4}$$

The instantaneous conduction heat transfer through the thin-film region is modeled by solving the radial conduction equation across the cylindrical thin film and equals

$$Q''_f = \frac{2\pi r_t k_l (T_w - T_{sat}) L}{\delta} \tag{5}$$

where L is the instantaneous length of the thin-film region. The time dependent thin-film thickness is modeled by equating the latent heat required to evaporate a differential cylindrical liquid volume of thickness $d\delta$ during time dt to the thin-film heat transfer. Substituting for Q''_f from Eq. (5), the differential form of the interfacial thickness is derived to be

$$\delta\,d\delta = \frac{-k_l (T_w - T_{sat})\,dt}{\rho h_{fg}} \tag{6}$$

Integrating the above equation from the start of the cycle ($t = 0$, $\delta = \delta_0$), the interfacial thickness is obtained as

$$\delta = \sqrt{\delta_0^2 - \frac{2k_l (T_w - T_{sat}) t}{\rho h_{fg}}} \tag{7}$$

Based on existing literature on boiling experiments from micro-structures, Webb and Haider [9] assumed the existence of liquid–vapor menisci oscillating back and forth inside the enhanced surface tunnels and proposed the following relationship for the driving pressure difference (Δp) during the expansion phase ($0 \leqslant t \leqslant 1/2f$),

$$\Delta p = (p_{sat,max} - p_{sat,min}) \sin(\pi f t) \tag{8}$$

The pressure in the vapor plug attains a maximum when the vapor embryo just protrudes from the surface pore

$$p_{sat,max} = p_{sat} + \frac{4\sigma}{D_p} \tag{9}$$

and the minimum pressure in the vapor plug occurs when the bubble growing at the top of the tunnel assumes the departure diameter

$$p_{sat,min} = p_{sat} + \frac{4\sigma}{D_b} \tag{10}$$

The maximum driving differential pressure becomes

$$\Delta p_{max} = p_{sat,max} - p_{sat,min} = 4\sigma\left(\frac{1}{D_p} - \frac{1}{D_b}\right) \tag{11}$$

The streamwise momentum equation for the oscillatory motion of the liquid slug in the tunnel reduces to

$$\frac{\partial u}{\partial t} = \frac{-\Delta p_{max} \sin(\pi f t)}{\rho x_m} + \frac{v}{r}\frac{\partial}{\partial r}\left(r\frac{\partial u}{\partial r}\right) \tag{12}$$

where x_m represents the mean length of the liquid slug inside the tunnel. Webb and Haider [9] showed the assumption of inviscid flow inside the enhanced surface tunnels results in negligible error in the tunnel heat transfer prediction. Neglecting the viscous term in the momentum equation (Eq. (12)) results in the following solution for the velocity

$$u = \left(\frac{\Delta p_{max}}{\pi f \rho x_m}\right) \cos(\pi f t) \tag{13}$$

The instantaneous length of the thin-film region during the expansion phase is modeled using

$$\frac{dL}{dt} = 2u \Rightarrow L = L_{max} \sin(\pi f t) \tag{14}$$

where L_{max} is the maximum expansion length of the vapor zone.

The pressure drop across the slug during the contraction phase is modeled as ($1/2f < t \leqslant 1/f$)

$$\Delta p = \Delta p_{max} \cos(\pi f t) \tag{15}$$

with the solution of the slug velocity in the contraction phase given by

$$u = -\left(\frac{\Delta p_{max}}{\pi f \rho x_m}\right) \sin(\pi f t) \tag{16}$$

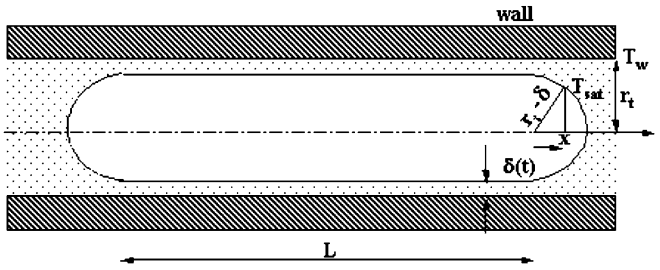

Fig. 3. Geometry of vapor plug inside the tunnel used for computing Q''_m and Q''_f. Axial conduction is assumed to be negligible.

Application of the above velocity field results in the length of the thin-film region in the contraction phase as

$$L = L_{\max}(1 + \cos(\pi f t)) \tag{17}$$

The maximum length of the vapor expansion ($L_{\max}$) is calculated by equating the mass of vapor formed to the mass of the departing bubble. The increase in the mass of the vapor as it expands from the minimum vapor pressure ($p_{\min}$) to the maximum vapor pressure ($p_{\max}$) is given by

$$m_{\max} - m_{\min} = \frac{1}{h_{\mathrm{fg}}} \int_0^{1/2f} (2Q''_{\mathrm{m}} + Q''_{\mathrm{f}})\,\mathrm{d}t \tag{18}$$

Assuming the heat transfer rate during the expansion and contraction phase of the vapor plug to be the same with small variations in the vapor density, Eq. (18) reduces to

$$m_{\max} - m_{\min} = \rho_{\mathrm{v}}(V_{\max} - V_{\min}) = \frac{\pi}{12}\rho_{\mathrm{v}} D_{\mathrm{b}}^3 \tag{19}$$

The minimum ($V_{\min}$) and maximum ($V_{\max}$) volume of the vapor plug is obtained from a geometrical analysis of the system to be

$$V_{\min} = \frac{4}{3}\pi(r_{\mathrm{t}} - \delta_0)^3 \tag{20a}$$

$$V_{\max} = \pi(r_{\mathrm{t}} - \delta)^2 L_{\max} + \frac{4}{3}\pi(r_{\mathrm{t}} - \delta)^3 + \frac{2}{3}\pi\left(\frac{D_{\mathrm{p}}}{2}\right)^3 \tag{20b}$$

Substituting Eq. (20) in Eq. (19) results in

$$L_{\max} = \frac{D_{\mathrm{b}}^3}{12(r_{\mathrm{t}} - \delta)^2} - \frac{4}{3(r_{\mathrm{t}} - \delta)^2}\left\{(\delta_0^3 - \delta^3) - 3r_{\mathrm{t}}(\delta_0^2 - \delta^2) + 3r_{\mathrm{t}}^2(\delta_0 - \delta) - \frac{D_{\mathrm{p}}^3}{16}\right\} \tag{21}$$

2.4. Modeling initial film thickness

The initial film thickness is modeled using lubrication theory and assumes the motion of vapor plug in the expansion phase would result in a thin liquid film along the tunnel walls. The liquid film thickness, δ_0, lubricated by the two menisci, each receding with velocity u_0 in the circular tunnel of radius r_{t} is given by [16]

$$\frac{\delta_0}{r_{\mathrm{t}}} = 1.3375 Ca^{2/3} \tag{22}$$

where Ca ($=\mu u_0/\sigma$) is the capillary number. The growth of the vapor region at the beginning of the expansion phase is heat diffusion controlled. Thus, the initial velocity u_0 at the beginning of the expansion phase is obtained by equating the initial heat transfer to the plug to the latent heat corresponding to the vapor generation rate, resulting in [16]

$$u_0 = \frac{1}{2}\left(\frac{\mathrm{d}L}{\mathrm{d}t}\right)_{t=0} = \frac{4k_{\mathrm{l}}(T_{\mathrm{w}} - T_{\mathrm{sat}})}{\rho_{\mathrm{v}} h_{\mathrm{fg}} r_{\mathrm{t}}} \sqrt{\frac{r_{\mathrm{t}}}{2\delta_0}} \tan^{-1}\sqrt{\frac{r_{\mathrm{t}}}{2\delta_0}} \tag{23}$$

The initial film thickness δ_0 is obtained by solving Eqs. (22) and (23) iteratively till convergence.

2.5. Modeling external heat transfer

Haider and Webb [17] developed a sub-model for external convection based on the model of Mikic and Rohsenow [18] for boiling from a plain surface. Haider and Webb's model included a transient term to account for the convection in the wake of the departing bubble. The model assumes that the beginning of the bubble cycle is dominated by transient conduction, and the final part is dominated by micro-convection caused by the wake of the departing bubble and expresses the external heat flux as

$$Q''_{\mathrm{ex}} = 2\sqrt{\pi k_{\mathrm{l}}\rho_{\mathrm{l}} c_{p\mathrm{l}} f}\, D_{\mathrm{b}}^2 n_{\mathrm{s}} \Delta T_{\mathrm{sup}} \left\{1 + \left(\frac{0.66\pi c}{Pr^{1/6}}\right)^2\right\}^{1/2} \tag{24a}$$

where the empirical constant of $c = 6.42$, was curve fitted from the Chien and Webb [19] and Nakayama et al. [15] bubble formation data. Ramaswamy et al. [11] found a constant value for the empirical constant c resulted in significant over-prediction of the external heat flux at high wall superheats and they replaced it with a third order polynomial function of the wall superheat given by

$$c = a_0 + a_1(\Delta T_{\mathrm{sup}}) + a_2(\Delta T_{\mathrm{sup}})^2 + a_3(\Delta T_{\mathrm{sup}})^3 \tag{24b}$$

where the constants are $a_0 = 6.58$, $a_1 = -1.1612/^{\circ}\mathrm{C}$, $a_2 = 0.0782/^{\circ}\mathrm{C}^2$ and $a_3 = -0.0018/^{\circ}\mathrm{C}^3$. Eq. (24) predicted the data listed in Haider and Webb [17] and Ramaswamy et al. [7] within ±40% for all data points [20].

2.6. Modeling nucleation site density

The nucleation site density in the present model is predicted through a correlation, with the empirical constants determined from the nucleation site density data reported in literature. The liquid–vapor plug dynamics inside the tunnel of structured surfaces that govern the nucleation site density depends on the geometric parameters and the wall superheat. The geometric factors that determine the total number of bubble generated are the pore diameter (D_{p}), tunnel radius (r_{t}) and the total surface pore density (N_{s}). The nucleation density correlation is obtained by curve fitting the FC-72 [7] and R-123 [6] experimental data as

$$n_{\mathrm{s}} = C(\Delta T)^{x1}(N_{\mathrm{s}})^{x2}(r_{\mathrm{t}})^{x3}(D_{\mathrm{p}})^{x4} \tag{25}$$

where the constants are

$$C = 1246.38, \quad x1 = 0.912, \quad x2 = 0.435,$$
$$x3 = 0.762, \quad x4 = -0.545$$

Fig. 4 shows the prediction of the nucleation density, using the correlation in Eq. (25), to be within ±30% of the data reported in literature.

2.7. Prediction procedure

Based on the equations outlined, the steps in predicting the parameters of boiling from structured surfaces are as follows:

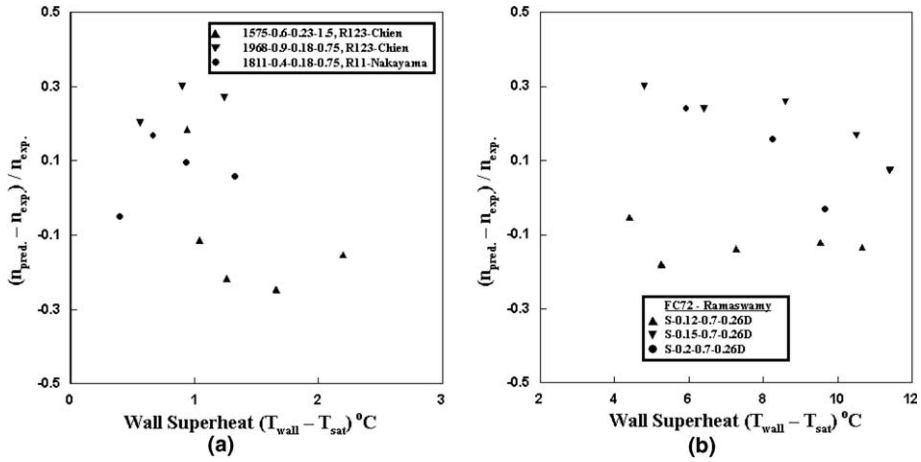

Fig. 4. Comparison of experimental nucleation site density with those predicted using correlation in Eq. (25).

(1) Calculate the bubble departure diameter (D_b) using the force balance as given by Eq. (1).
(2) Solve Eqs. (22) and (23) iteratively to get the initial film thickness (δ_0).
(3) Calculate the bubble departure frequency by solving Eq. (3), which can be expanded as

$$\int_0^{1/2f} (2Q_m + Q_f)_{exp}\,dt + \int_{1/2f}^{1/f} (2Q_m + Q_f)_{con}\,dt = \frac{\pi}{6}\rho_v h_{fg} D_b^3 \quad (26)$$

The first and second terms in Eq. (26) represent the latent heat transfer during the expansion and contraction phases respectively. The film heat transfer (Q_f) becomes zero on reaching the non-evaporating thickness (δ_{ne}).
(4) Calculate the nucleation site density by using Eq. (25).
(5) The total heat flux, which is the sum of the tunnel heat flux ($n_s Q''_t$) and the external heat flux (Q''_{ex}), is obtained from Eqs. (3) and (24).

3. Results of semi-analytical model

The semi-analytical model described in the previous section was used to predict the bubble departure diameter, bubble frequency, nucleation site density and the total heat flux for boiling from porous enhanced surfaces, and compared with experimental data reported in the literature. Table 1 briefly summarizes the geometric details of the various studies used in the validation of the semi-analytical model. The nomenclature used in identifying the studies is similar to those used by the investigators in reporting their results (Fig. 5), with H_t referring to the sub-surface tunnel height, D_p denoting the pore diameter and P_p representing the pore pitch. For example, Chien's structure 1968–0.9–0.18–0.75 refers to 1968 fins/m, 0.9 mm tunnel height, 0.18 mm pore diameter and 0.75 mm pore pitch. Similarly, Ramaswamy's structure S–0.2–1.0–0.26W refers to a structured surface in silicon with 0.2 mm pore diameter, 1.0 mm pore pitch and 0.26 mm tunnel height. The last letter identifies the method used for making the enhancement structures, in this case 'W' signifying wet-etch process.

3.1. Prediction of the departure diameter

A comparison of the predicted and experimental values for bubble departure diameter is shown in Fig. 6. The results show very good agreement, with the absolute error being within ±20%. The present model does not capture the observed decrease in departure diameter [4,19] for low wall superheats in the range 1–3 °C. Zuber [21] suggested that for very low wall superheats, the bubble departure is a function of the buoyancy and surface tension forces only. Therefore, an increase in wall temperature

Table 1
Geometrical details for the parametric studies in literature

Investigators (Nomenclature)	Fluid	Tunnel pitch (mm)	Tunnel height (mm)	Pore diameter (mm)	Pore pitch (mm)
Nakayama et al. [4] (Fins/m-H_t–d_p–P_p)	Water	0.5–0.6	0.5–0.62	0.08–0.2	0.6–0.72
	R-11	0.55	0.4	0.04–0.15	0.7
	Liquid nitrogen	0.4	0.4–0.56	0.03–0.2	0.72
Chien and Webb [6] (Fins/m-H_t–d_p–P_p)	R-11, R-123 and R-22	0.5–0.72	0.5–1.5	0.12–0.28	0.75–0.3
Ramaswamy et al. [20] (Material-d_p–P_p–H_t)	FC-72	0.6–0.9	0.4–0.6	0.07–0.15	0.07–0.15

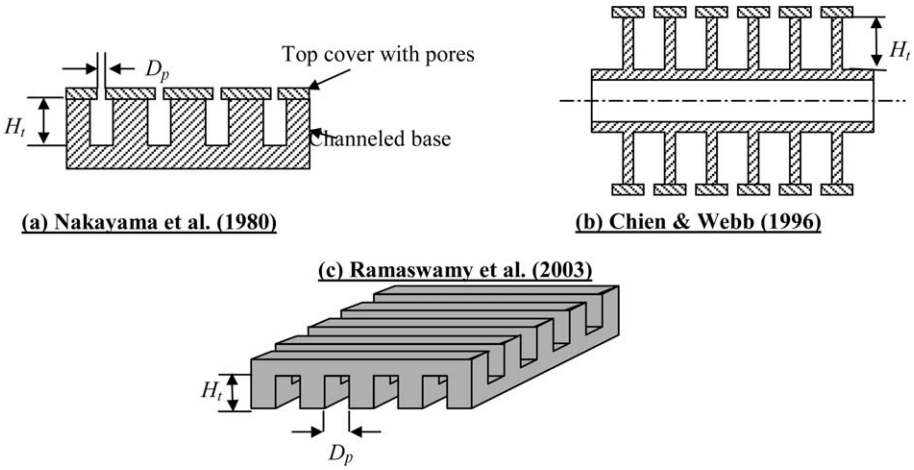

Fig. 5. Shows the enhancement structures reported in literature used for validating the semi-analytical model. The geometric parameters of the structures are summarized in Table 1.

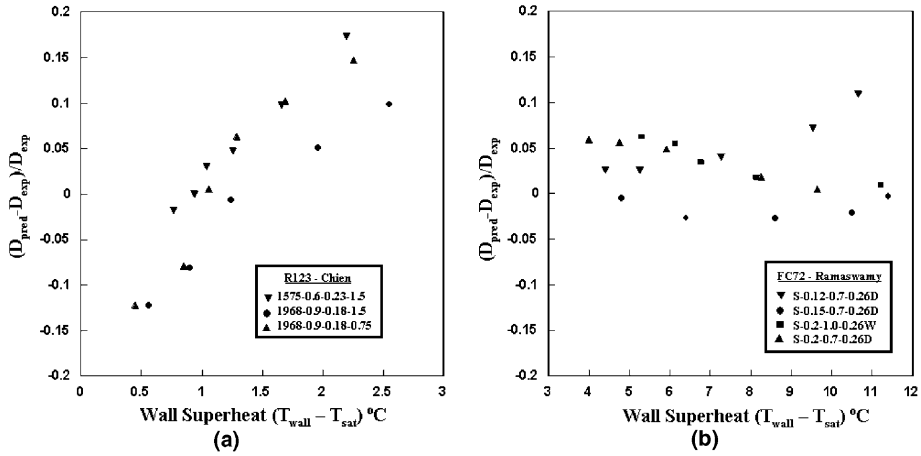

Fig. 6. Comparison of bubble departure diameter—prediction vs. experiments.

causes a reduction in surface tension forces, resulting in a decrease in the departure diameter. The present model does not account for temperature dependent surface tension effects and hence fails to predict the trends in bubble departure diameter variation at low wall superheats. However, as the wall superheat is increased further, dynamic forces start dominating the bubble growth and the variation in surface tension force with temperature becomes negligible in comparison.

3.2. Prediction of frequency

A comparison of the predicted values for frequency and experimentally observed values is shown in Fig. 7. The trends in variation of frequency with wall superheat are captured fairly accurately. The error in the prediction lies within a range of ±35%. The model predicts the frequency to increase monotonically with increase in wall superheat values. However, the experimental values of Ramaswamy et al. [7] show a reduction in the frequency at intermediate wall superheats. This was explained through the induced sweeping motion caused by the liquid return to the evaporator in their experimental set-up. The current model does not account for this phenomenon as such an analysis involves significant additional complexities that are beyond the scope of the present work.

3.3. Prediction of heat flux

A comparison of the predictions using the present model and experiments for structures used in Chien and Webb [19] and Nakayama et al. [4] is shown in Fig. 8a. The model predicts the heat flux variation with wall temperature within ±40% for all available data. Fig. 8b shows that the predicted heat transfer coefficients follow the trend observed in experiments. The heat transfer coefficient varies with heat flux to the power of 0.46, which implies that the heat flux varies with wall superheat to the power of 1.8. The exponent is higher than the value of 1.24 predicted for natural convection boiling but is less than Rohsenow's prediction for nucleate boiling, where the heat flux varies to the cube of wall superheat.

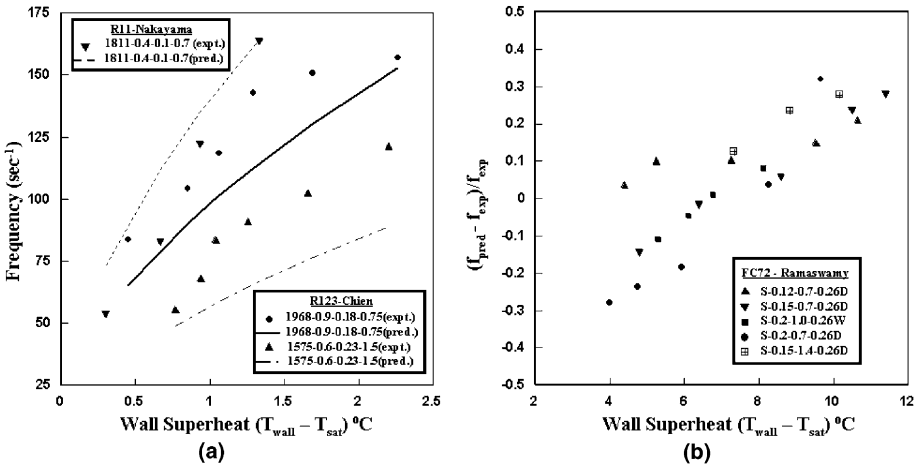

Fig. 7. Comparison of frequency—prediction vs. experiments.

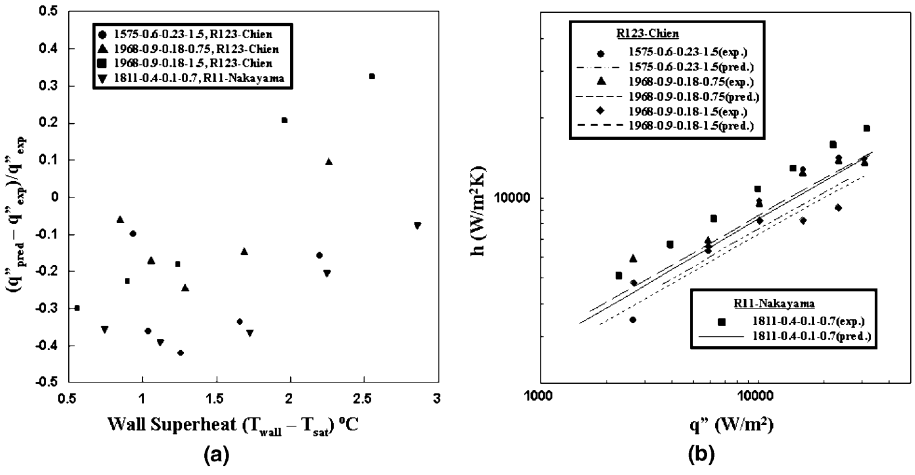

Fig. 8. Comparison of prediction vs. experiments for Chien's and Nakayama's structures (a) heat flux and (b) heat transfer coefficient.

Fig. 9a and b compare the model prediction with the experimental data obtained using Ramaswamy et al.'s [7] boiling enhancement structures with a pore size of 150 μm and 200 μm, respectively. The data show that the prediction for these structures was fairly accurate. The maximum error in prediction for the 150 μm and 200 μm

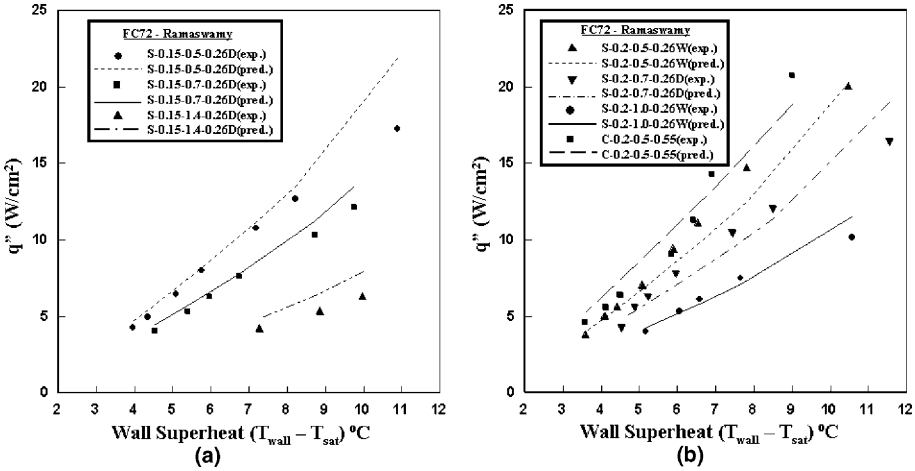

Fig. 9. Comparison of heat flux variation with wall temperature for Ramaswamy's structures of pore size (a) $D_p = 150$ μm and (b) $D_p = 200$ μm.

structure was within ±30%. The prediction error increases with increase in wall superheat, suggesting a possible transition in the boiling mode. Also, the present model was developed primarily for the isolated bubble regime and becomes invalid when bubbles departing the surface coalesce vertically or laterally.

3.4. Prediction of flat plate spreader performance

The above model for boiling from structured porous surfaces was used in predicting the thermal performance of a novel two-phase heat spreader [22] that employs an enhancement structure (Fig. 10). The single layer copper enhancement structure used in the spreader was similar to the porous structures used by Nakayama et al. [15]. The copper layer had rectangular channels (0.31 mm wide, 0.55 mm deep) cut on either side of the plate with a 0.71 mm pore pitch. The channels intersect to form square pores of 0.31 mm size, which act as sites for bubble nucleation.

The semi-analytical model requires as input the liquid saturation temperature (T_{sat}), along with the geometry of the enhanced surface and the fluid properties. At steady state, the condenser walls of the spreader plate are assumed to be at T_{sat}. The saturation temperature is resolved iteratively through a conduction model of the external condenser wall with peripheral fins, by satisfying the energy balance for a given heat input and external boundary conditions. Experiments were carried out without any liquid in the spreader plate and the data were used in arriving at the external convection heat transfer coefficients used in the conduction model. The liquid saturation temperature thus obtained is used as an input to the semi-analytical model to predict the wall temperature (T_{wall}). Fig. 11 shows a schematic of the algorithm used. Fig. 12 compares the

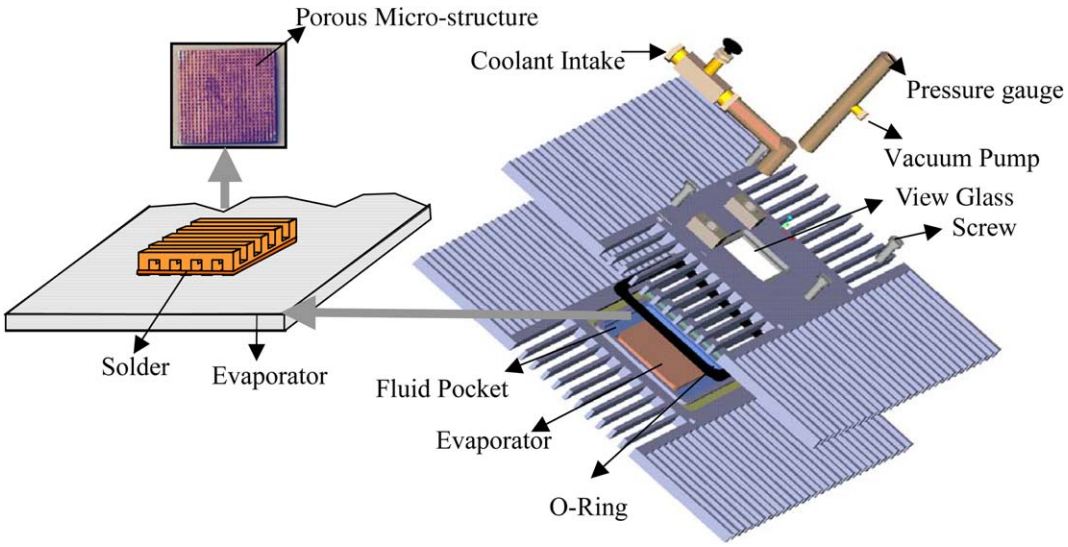

Fig. 10. Exploded view of the two-phase heat spreader with the enhancement structure attached to the evaporator section of the spreader plate.

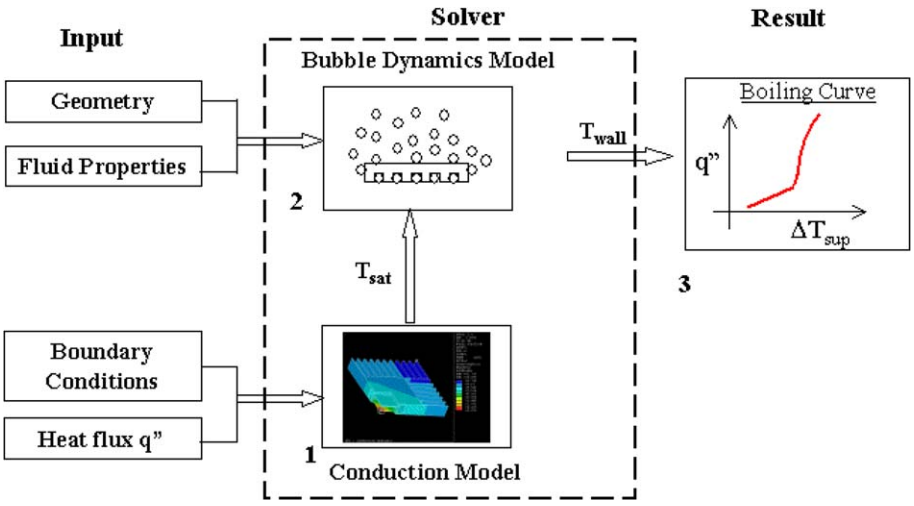

Fig. 11. Algorithm for the two-phase spreader thermal performance model based on the semi-analytical model for enhanced boiling.

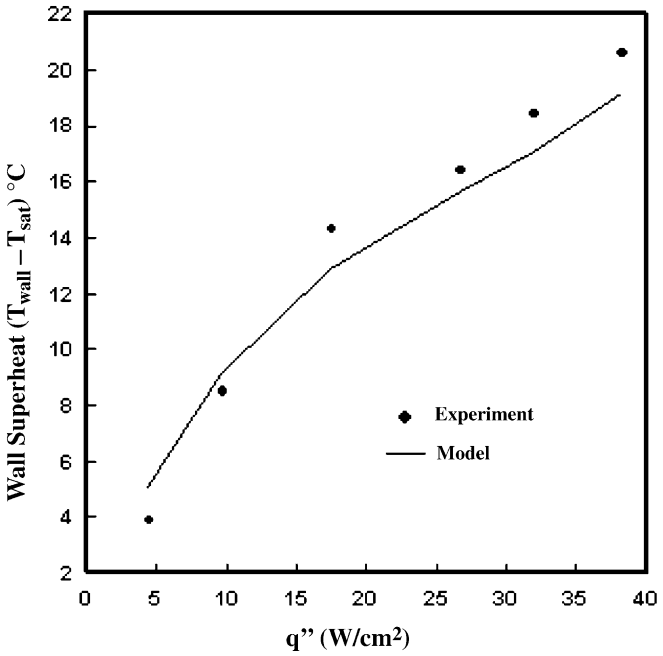

Fig. 12. Thermal performance predictions of the forced air-cooled (1 m/s) two-phase heat spreader.

prediction from the spreader model with the data obtained from the forced convection experiments using the copper spreader plate. The model captures the trends in thermal performance of the two-phase spreader plate with the maximum error in wall superheat prediction being 30%.

4. Conclusions

A semi-analytical model that predicts the bubble dynamics for boiling from structured porous surfaces has been developed for a range of wall superheat (0–12 °C) and validated against existing experimental data. The salient improvements over existing models and conclusions based on the predictions are

(1) Previously existing models of 'suction–evaporation' mode of boiling from enhanced surfaces have been developed on Hamaker constant values that are nearly 6–8 orders of magnitude higher than actual ones. These models are very sensitive to the Hamaker constant and fail to predict correctly the observed bubble dynamics on using the correct value. Also, the existing models of 'suction–evaporation' mode fail to explain the observed enhancement from enhancement surfaces with circular tunnels.
(2) A modified model for 'flooded' mode boiling regime was developed with the inclusion of dynamic forces in the prediction of bubble departure diameter. The bubble departure predictions were within ±20%. The error in frequency predictions was within ±35%.
(3) A correlation for nucleation site density was developed based on wall superheat and structure geometry properties.
(4) The heat flux predictions were found to be within ±30% with the model capturing the trends fairly well.
(5) The boiling model was subsequently used in predicting the thermal performance of a novel two-phase heat spreader that employs enhancement structures in the evaporator section of the spreader plate. The temperature predictions from the semi-analytical model agreed within an accuracy of ±30% of experimental results even at higher wall superheats (>12 °C).

Acknowledgement

The authors acknowledge support for this work by the Semiconductor Research Corporation through contract 99-NJ-649.

Appendix

The expressions used in calculating the bubble departure diameter (Eq. (1)) are listed below:

(a) Unsteady growth force: The expression for an inertia driven growth force is given as

$$F_{ug} = 10\rho_l \pi \dot{R}^2 R^2 \tag{A1.1}$$

(b) Buoyancy force: The buoyancy force on a bubble is given as

$$F_B = (\rho_l - \rho_v) g V_b \tag{A1.2}$$

where V_b is the truncated bubble volume at departure and is given as

$$V_b = \frac{\pi}{3}\left(\frac{D_b^3}{4} + \frac{D_b^2}{4}\sqrt{D_b^2 - D_p^2} + \frac{D_p^2}{8}\sqrt{D_b^2 - D_p^2}\right) \tag{A1.3}$$

(c) Surface tension force: The surface tension force is given as

$$F_{st} = \sigma \pi D_p \sin\theta \tag{A1.4}$$

where the contact angle θ is evaluated as

$$\theta = \sin^{-1}\left(\frac{D_p}{D_b}\right) \tag{A1.5}$$

(d) Bubble inertia force: The expression for bubble inertia force, as used by Sharma [23]

$$F_{bi} = m\frac{dv_g}{dt} + v_g \frac{dm}{dR}\frac{dR}{dt} \tag{A1.6}$$

reduces to

$$F_{bi} = \rho_v \frac{\pi}{3}\dot{R}^2 \left\{\frac{3D_b^2}{4} + \frac{1}{4}\left(\frac{3D_b^3 - 2D_b D_p^2}{\sqrt{D_b^2 - D_p^2}} + \frac{D_b D_p^2}{2\sqrt{D_b^2 - D_p^2}}\right)\right\} \tag{A1.7}$$

for a linear bubble growth rate with the velocity at the bubble center given by $v_g = dR/dt$.

(e) Lift force: The departing bubble has a tendency to drag the next bubble growing at the same pore. The lift force due to wake of the departing bubble is modeled as

$$F_L = 2.4\pi\rho_l(D_b\dot{R})^2 \quad \text{(A1.8)}$$

References

[1] R.L. Webb, The evolution of enhanced surface geometries for nucleate boiling, Heat Transfer Eng. 2 (1981) 46–69.

[2] A.E. Bergles, Enhanced heat transfer: endless frontier, or mature and routine? Enhanced Heat Transfer 6 (1999) 79–88.

[3] K. Cornwell, B.G. Nair, T.D. Patten, Observation of boiling in porous media, Int. J. Heat Mass Transfer 19 (1976) 236–238.

[4] W. Nakayama, T. Daikoku, H. Kuwahara, T. Nakajima, Dynamic model of enhanced boiling heat transfer on porous surfaces Part I: experimental investigation, J. Heat Transfer 102 (1980) 445–450.

[5] J. Arshad, J.R. Thome, Enhanced boiling surfaces: heat transfer mechanism mixture boiling, in: Proceedings of ASME-JSME Thermal Engeineering Joint Conference, vol. 1, 1983, pp. 191–197.

[6] L.H. Chien, R.L. Webb, Visualization experiments of pool boiling on enhanced surfaces, Exp. Therm. Fluid Sci. 16 (1998) 332–341.

[7] C. Ramaswamy, Y. Joshi, W. Nakayama, W.B. Johnson, High speed visualization of boiling from an enhanced structure, Int. J. Heat Mass Transfer 45 (2002) 4761–4771.

[8] W. Nakayama, T. Nakajima, S. Hirasawa, Heat Sink Studs having Enhanced Boiling Surfaces for Cooling Microelectronic Components, ASME Paper No. 84-WA/HT-89, 1984.

[9] R.L. Webb, S.I. Haider, An analytical model for nucleate boiling on enhanced surfaces, in: V.K. Dhir, A.E. Bergles (Eds.), Pool and External Flow Boiling, 1992, pp. 345–360.

[10] L.H. Chien, R.L. Webb, A nucleate boiling model for structured enhanced surfaces, Int. J. Heat Mass Transfer 41 (1998) 2183–2195.

[11] C. Ramaswamy, Y. Joshi, W. Nakayama, W.B. Johnson, Semi-analytical model for boiling from enhanced structures, Int. J. Heat Mass Transfer 46 (2003) 4257–4269.

[12] S. Dasgupta, J.A. Schonberg, P.C. Wayner, investigation of an evaporating extended menisci based on the augmented Young–Laplace equation, J. Heat Transfer 115 (1993) 201–208.

[13] J. Israelachvili, Intermolecular and Surface Forces, Academic Press, Florida, 1991.

[14] C.-D. Ghiu, Y. Joshi, W. Nakayama, Visualization study of pool boiling from transparent enhanced surfaces, in: Proceedings of the 35th National Heat Transfer Conference, Anaheim, June 2001 pp. 697–704.

[15] W. Nakayama, T. Daikoku, H. Kuwahara, T. Nakajima, Dynamic model of enhanced boiling heat transfer on porous surfaces, Part II: analytical modeling, J. Heat Transfer 102 (1980) 451–456.

[16] S.I. Haider, A Theoretical and Experimental Study of Nucleate Pool Boiling Enhancement on Structured Surfaces, Ph.D. Thesis, The Pennsylvania State University, University Park, PA, 1994.

[17] S.I. Haider, R.L. Webb, A transient micro-convection model of nucleate pool boiling on plain surfaces, Int. J. Heat Mass Transfer 40 (1997) 3675–3688.

[18] B.B. Mikic, W.M. Rohsenow, A new correlation of poll boiling data and effect of heating surface characteristics, J. Heat Transfer 91 (1969) 245–250.

[19] L.H. Chien, R.L. Webb, Measurement of bubble dynamics on an enhanced boiling surface, Exp. Therm. Fluid Sci. 16 (1998) 177–186.

[20] C. Ramaswamy, A Compact Two-Phase Thermosyphon Employing Microfabricated Boiling Enhancement Structures, Ph.D. Thesis, University of Maryland, College park, MD, 1999.

[21] N. Zuber, Nucleate boiling—the region of isolated bubbles—similarity with natural convection, Int. J. Heat Mass Transfer 6 (1963) 53–56.

[22] S. Murthy, Y. Joshi, W. Nakayama, Single chamber compact two-phase heat spreaders with micro-fabricated boiling enhancement structures, IEEE Trans. Compon. Packag. Technol. 25 (2002) 156–163.

[23] P.R. Sharma, Determination of heat transfer rates in nucleate pool boiling of pure liquids for a wide range of pressure and heat flux, in: Proceedings of the 11th International Heat Transfer Conference, vol. 2, Kyongiu, South Korea, 1998, pp. 467–472.